Incorporation of Bi-Atoms in InP Studied at the Atomic Scale by Cross-Sectional Scanning Tunneling Microscopy

C. M. Krammel,[1,*] M. Roy,[2] F. J. Tilley,[2] P. A. Maksym,[2] L. Y. Zhang,[3] P. Wang,[3] K. Wang,[3] Y. Y. Li,[3] S. M. Wang,[3,4] and P. M. Koenraad[1]

[1] *Department of Applied Physics, Eindhoven University of Technology, Eindhoven 5612 AZ, The Netherlands*
[2] *Department of Physics and Astronomy, University of Leicester, University Road, Leicester LE1 7RH, United Kingdom*
[3] *State Key Laboratory of Functional Materials for Informatics, Shanghai Institute of Microsystem and Information Technology, Chinese Academy of Sciences, Shanghai 200050, China*
[4] *Department of Microtechnology and Nanoscience, Chalmers University of Technology, 41296 Göteborg, Sweden*

(Dated: July 10, 2017)

We show the potential of cross-sectional scanning tunneling microscopy to address structural properties of dilute III-V-bismides by investigating Bi:InP. Bismuth atoms down to the second monolayer below the {110} InP surfaces, which give rise to three classes of distinct contrast, are identified with the help of density functional theory calculations. Based on this classification the pair correlation function is used to quantify the ordering of Bi-atoms on the long range. In a complementary short ranged study, we investigate the Bi-ordering at the atomic level. An enhanced tendency for the formation of first nearest neighbor Bi-pairs is found. In addition, the formation of small Bi-clusters is observed whose geometries appear to be related to strong first nearest neighbor Bi-pairing. We also identify growth related crystal defects, such as In-vacancies, P-antisites, and Bi-antisites.

PACS numbers: 68.37.Ef, 81.15.Hi, 71.55.Eq, 66.35.+a
Keywords: scanning tunneling microscopy, molecular beam epitaxy, III-V semiconductors, bismuth doping, density functional theory calculations

I. INTRODUCTION

Highly mismatched Bi-containing III-V semiconductors have attracted a lot of attention due to their unusual optical and electronic properties.[1–4] However, state of the art dilute III-V-bismides still suffer, despite their strong innovative potential, from a number of problems, which are related to short ranged ordering and defect formation. There is a strong need for non-averaging techniques that can address these questions in real space at the atomic level. We propose cross-sectional scanning tunneling microscopy (X-STM) as an ideal tool to meet this challenge.

Until now, most experimental studies of the MBE growth of highly mismatched III-V-bismides, as $GaAs_{1-x}Bi_x$,[5,6] $InAs_{1-x}Bi_x$,[7,8] and $InP_{1-x}Bi_x$[4,9,10] are limited to the improvement of the growth conditions and the optical characterization of their material properties. In contrast to other highly mismatched III-V-bismides, which are grown at low temperatures by MBE, Bi:InP shows additional strong optical transitions at lower energies than the commonly observed band-to-band transitions.[4,9,11] Deep level transient spectroscopy (DLTS) measurements have suggested that this is related to Bi-clustering.[12]

The few structural studies, which investigate the microscopic properties of bismides are solely limited to Bi-doped GaAs. These investigations are based on averaging techniques such as scanning transmission electron microscopy (STEM) and extended X-ray absorption fine-structure spectroscopy measurements (EXAFS),[13,14] which by definition cannot entirely grasp the structural characteristics of bismides at the atomic level. In contrast, X-STM can be used to determine the local atomic structure.

In this paper, we set the stage for future X-STM studies in the field of dilute III-V-bismides by carefully studying Bi incorporation in InP based bulk layers and quantum wells (QWs). The growth of the investigated samples, the X-STM measurements, and the DFT calculations are described in section II. In section III A, we identify the main Bi related features by X-STM and complementary density functional theory (DFT) calculations. Based on this classification, we analyze in section III B the ordering of Bi-atoms and quantify their tendency towards pairing as well as clustering. Our investigations of crystal defects in InP:Bi are detailed in section III C. At the end in section IV we summarize our work.

II. EXPERIMENTAL AND COMPUTATIONAL METHODS

A. Growth of Bi:InP

In this study, two Bi doped InP samples A and B are analyzed by X-STM to characterize their structural properties. Sample A consists of a 420 nm thick Bi:InP bulk layer (F1) with an intended Bi content of 1.2 %. Sample B contains three sets of stacked

Bi:InP(15 nm)/InP(20 nm) QW multilayers with intended Bi concentrations of 0.1 % (QW 1), 0.5 % (QW 2) and 1.0 % (QW 3). This multilayer region is followed by a 150 nm thick Bi:InP bulk layer (F2) with an intended Bi concentration of 2.4 %. The three different Bi:InP/InP QWs 1, 2, and 3 are used to investigate the atomic structure of the Bi-atoms and the role of crystal defects. The Bi distribution is studied at layers F1 and F2. Details about the growth of samples A and B are provided in section I of the supplementary material.

B. X-STM investigations

The X-STM measurement on sample A was performed at room temperature in an Omicron STM-1 and the work on sample B was carried out at 5 K in an Omicron low temperature STM. The samples were cleaved *in situ* at pressures below 4×10^{-11} mbar, revealing clean and atomically flat {110} surfaces. In both systems electrochemically etched polycrystalline W-tips were used. Both Bi:InP samples were studied in constant-current mode over a wide range of sample voltages. In filled state images sample voltages from -1.9 V to -2.8 V and in empty state images sample voltages from 1.5 V to 2.4 V were used.

C. Density functional theory calculations

DFT calculations were performed within the local density approximation using the ABINIT software package[15,16] and the Fritz-Haber-Institute (FHI) norm-conserving pseudopotentials.[17]

126 atom super-cells with a 3×3 surface periodicity were used, with a cut off energy for the plane wave basis set, E_{cut}, of 30 Ry and a $4 \times 4 \times 1$ $\boldsymbol{k}$-grid.[18] The super-cells are separated by a 12 Å vacuum gap and the system was allowed to fully relax with a tolerance on the forces of 1×10^{-4} hartrees per bohr.

After relaxation, constant height STM images were calculated using the local density of states (LDOS) of the system following the Tersoff-Hamman model[19,20]. This is based on the Bardeen theory of tunneling[21] and gives the tunneling current $I(V_{bias}, \boldsymbol{r})$ in the form

$$I(V_{bias}, \boldsymbol{r}) \propto \int_{E_{\mathrm{BE}}}^{E_{\mathrm{BE}}+eV_{bias}} \rho_{\mathrm{LDOS}}(\boldsymbol{r}, E) dE, \qquad (1)$$

where ρ_{LDOS} is the local density of states, E_{BE} is the band edge energy and V_{bias} is the applied bias voltage. For filled state imaging we took E_{BE} to be the energy of the highest occupied state and for empty state imaging we took E_{BE} to be the energy of the lowest unoccupied state. V_{bias} is $+1$ eV for empty state imaging and -1 eV for filled state imaging. In all our calculations we took the tip position, $\boldsymbol{r}$, to be 4 Å above the position of the unperturbed surface phosphorous atoms.

Tests on the convergence of the DFT calculations are described in section II of the supplementary material.

III. RESULTS AND DISCUSSION

A. Classification of the main Bi related features

So far, the appearance of individual Bi-atoms in X-STM measurements on cleaved {110} surfaces of III-V semiconductors and the underlying contrast mechanism have not been properly addressed. This leads us first to a discussion of the most common Bi-related features, which are found in our X-STM measurements. For this purpose, QW 2 in sample B with an intended Bi concentration of 0.5 % is suited best. In QW 2 the Bi concentration is low enough to ensure that the Bi-atoms are well separated and high enough to ensure that enough of them appear in an atomically resolved X-STM image. Details of the investigated samples A and B and the growth conditions are given in section II of the paper and section I the supplementary material. Figure 1 shows atomically resolved filled state (a) and empty state (b) images of the same area of QW 2. Filled state and empty state imaging is essential to get a complete picture of the atomic structure of the Bi related features. Normally, empty group-III related states are addressed at positive sample voltage while at negative sample voltage contributions of the filled group-V related states are dominant.[22] The blue background in Figure 1 corresponds, depending on the applied sample bias, to the corrugation of the P-atoms and In-atoms of the InP matrix. Also a few crystal defects, see white circles, are observed, which are further discussed in section III C. The various localized bright features, as highlighted by green, orange, and red circles, are related to three different classes $(0, 1, 2)$ of isovalent Bi-atoms on substitutional P-sites ($\mathrm{Bi_P}$). Classes $(0, 1, 2)$ are on average found equally often in the X-STM measurements. This is further detailed in section III of the supplementary material. In the investigated samples, Bi is introduced under group-V rich MBE growth conditions. Under these circumstances, Bi is preferentially incorporated as an isovalent atom on group-V sites.[9]

The brightest atomic-like features, whose maxima coincide in the filled state X-STM image of Figure 1 (a) with regular lattice sites of the P-corrugation, are referred to as class (0). In contrast to the atomic structures in class (0), class (1) is characterized by much weaker features, which cover a rectangle of four P-corrugation maxima in the surface. The elements of class (2) are again located on a single atomic position of the P-corrugation and are brighter than class (1).

In the corresponding empty state X-STM image, which is shown in Figure 1 (b), the appearance of elements from class (0) is barely changed. However, the center of these features lies here in between the In corrugation, while in filled state images it falls on a corrugation maximum of the P-sublattice. Interestingly, the situation is dif-

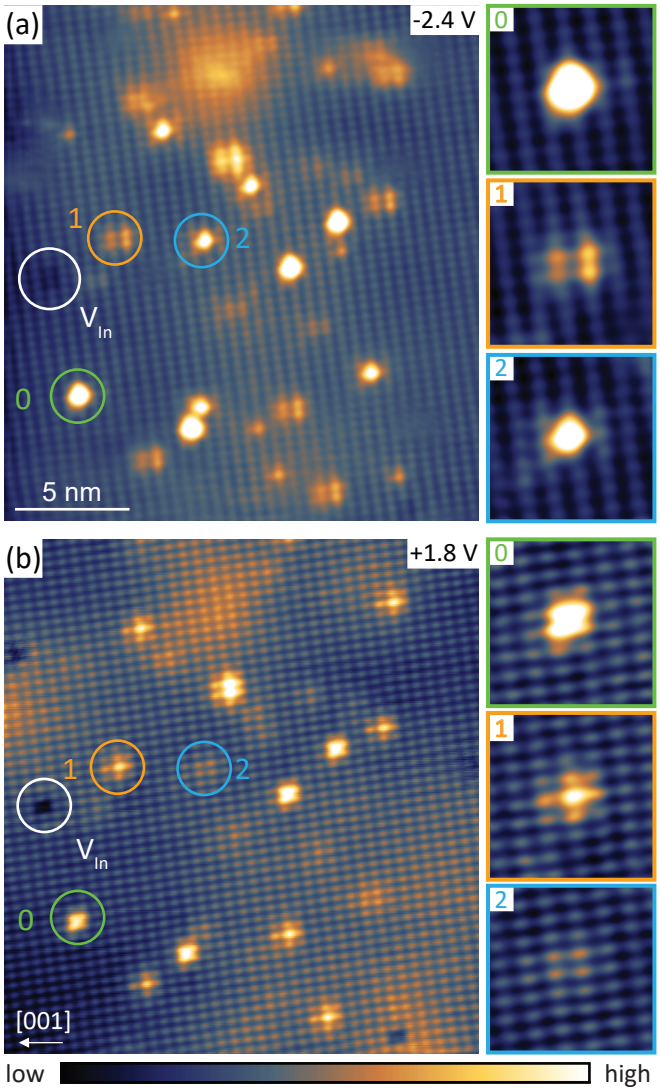

FIG. 1. (Color online) High resolution filled state (a) and empty state (b) X-STM images, which resemble the group-V (P, Bi) and the group-III (In) sublattices, respectively. Both images are taken from the same area of QW 2 in sample B using a tunnel current set point of $I_T = 30$ pA. The sample voltages are indicated in the upper right corners of the large images. The color scales of images (a, b) are independently adjusted for best visibility. Three different classes of features $(0, 1, 2)$ related to Bi-atoms down to the second layer below the cleavage plane are identified. Magnified portions of the areas highlighted by the circles are shown to the right of (a) and (b) in boxes with correspondingly colored frames and numbering. All magnifications are shown in the same color scale. The dark contrast, marked with a white circle, is related to a In-vacancy (V_{In}). The growth direction is indicated by an arrow in (b).

ferent for class (1), which, in filled state images, covers four P-corrugation maxima. In empty state images these features become brighter and appear to be mainly localized on a single maximum of the In-corrugation. Class (2), which is in filled state images atomic like, behaves in the opposite way to class (1). The class (2) features loose brightness compared to filled state images and are distributed over several In-sites.

The height changes of the STM tip originate in electronic and topographic effects, which are hard to quantify experimentally. This makes it difficult to clarify the origin of these three Bi-related classes solely based on experimental observations. Therefore, we performed first-principles DFT calculations for isovalent Bi_P-atoms in the first three layers of a (110) InP slab. Details of the simulation parameters and convergence tests are given in section II C and section II of the supplementary material. In the first column of Figure 2, energy integrated LDOS maps of the filled VB states, which represent the group-V sublattice, are shown for Bi atoms down to the second layer below (110) surface $(0, 1, 2)$. The second column represents the energy integrated LDOS maps of the empty CB states, which are associated with the group-III sublattice. Because of the inverse exponential dependence of the tunnel current on the tip-sample distance in the experiment, the integrated LDOS maps, which are proportional to the tunnel current, are presented in a logarithmic scale. A side view of the underlying (110) surface is provided in the third column. The distorted lattice sites are given by colored disks and their unperturbed positions are marked by empty circles. The (110) surface of the pure InP slab, which serves as origin for the z-scale in the ball-and-stick diagrams, is indicated by a dashed line.

The DFT calculation shows that a Bi_P-atom in the surface (0) relaxes as a consequence of its large effective size compared to a P-atom and occupies a position where it stands out of the surrounding relaxed surface [Figure 2 (g)]. The vertical displacement of the Bi-atom gives in the energy integrated LDOS maps rise to an atomic-like feature, which is located on the group-V corrugation or between the group-III corrugation [Figures 2 (a, d)]. This pattern is in good agreement to class (0) in Figure 1.

One layer below the surface (1), a Bi-atom bonds to four P-atoms in the surface [Figure 2 (h)], which experience only a weak displacement out the surface plane. Furthermore, the DFT simulation points towards a symmetry breaking along the [001] direction, which is induced by the geometry of the relaxed (110) surface. In this way one of the two pairs of P-atoms, which are oriented along the $[1\bar{1}0]$ direction, is shifted less upwards than the other P-pair [Figure 2 (h)]. These modifications of the surface are in good agreement with the slight asymmetry of the dumbbell-like structures of class (1), which are observed in experimental filled state X-STM images [Figure 1 (a)]. However, the contrast in the energy integrated LDOS map of the filled VB states [Figure 2 (b)] is not as pronounced as in the experiment. This suggests the model has minor deficiencies, which become particularly evident at weaker features. Unlike four P atoms, only one In atom in the surface is shifted into a

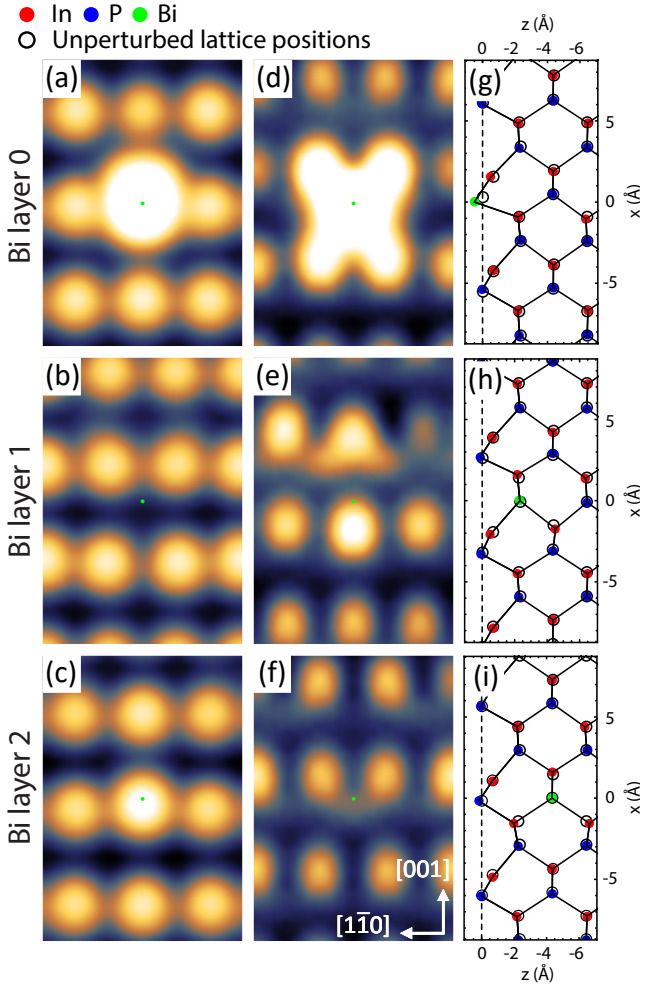

FIG. 2. (Color online) Energy integrated LDOS maps of the filled VB states (a, b, c) and empty CB states (d, e, f) for Bi_P-atoms down to the second layer below the (110) InP surface, which give rise to three classes of feature (0,1,2). The simulated X-STM images (first and second column) are plotted in a logarithmic scale and the Bi positions are indicated by a green dot. A side view of the relaxed InP (110) surface for classes (0,1,2) is shown in the third column (g, h, i). In the ball-and-stick plots, the In-, P-, and Bi-atoms are represented by red, blue, and green disks, respectively. The unperturbed lattice positions are marked by empty circles and the position of the (110) surface is indicated by a dashed line.

higher z-position [Figure 2 (h)]. The displacement of the In atom along the z-axis is stronger than for the four P atoms. This gives rise to a pronounced point-like contrast in the energy integrated LDOS map of the empty CB states [Figure 2 (e)], which is in good agreement to experimental images of class (1) at positive voltages [Figure 1 (b)].

For a Bi-atom in the second layer (2) below the surface, primarily one P-atom in the surface is affected, which relaxes into a higher z-position [Figure 2 (i)]. This displacement is weaker than for a Bi-atom in the surface. Accordingly, we get in the energy integrated LDOS map of the filled CB states a second atomic-like feature [Figure 2 (c)], which is less pronounced than in the first case. The In-atoms in the surface are hardly shifted into a higher z-position by the second layer Bi-atom. Therefore, the contrast is weakened in the energy integrated LDOS map of the empty CB states [Figure 2 (f)]. This is consistent with the behavior of class (2) in the experimental X-STM images (Figure 1).

The DFT calculations allow for a better understanding of the origin of the different Bi related classes as they provide a link between the X-STM images and the geometry of the (110) surface. At high sample voltages, the contrast of Bi-atoms in the first three {110} InP surface layers, classes $(0, 1, 2)$, goes primarily back to structural modifications of the relaxed surface. Electronic effects appear to be less important. Bi is the largest stable group-V element and contrasts similar to those shown in Figure 1 can be expected for Bi-atoms in the first three {110} layers of any binary III-V zinc-blende semiconductors. However, the strength of the three classes (0,1,2) of Bi related contrasts is supposed to decrease in alloys with larger anions, which may cause difficulties in the recognition of Bi related features in antimonides. This geometrical interpretation can be seen as an experimental confirmation and extension of the theoretical work of Tilley et al. in Ref. 18 on the structural modification of the (110) GaAs surface by isovalent dopants from groups III and V. There, it has been shown that the relaxed position of isovalent impurities in the (110) surface depends on the effective size of the involved elements. Bigger/smaller atoms than the ones they are replacing relax into a position above/below the surface, which leads to atomic-like bright/dark contrasts in STM measurements.

Even though experiment and calculation are in good qualitative agreement, there are some differences between them. This can have many possible causes. For instance, the tip has in the experiment its own electronic structure, which also affects the tunnel current. However, the contributions from the tip are at a fixed sample voltage always the same. Therefore, it is primarily the changes in the LDOS of the sample, which dominates the local variations of the tunnel current in a STM image. Another important factor is the electric field, which is applied between tip and sample. Especially, the low charge density of semiconducting samples causes a part of the electric field to drop off in the sample. This effect is known as tip induced band bending (TIBB), which mainly affects the energy scale in X-STM measurements.[23] Therefore, the TIBB is more important for the interpretation of tunneling spectra than for the general discussion of X-STM images under normal conditions. In addition, the electric field can also deform the surface states of the sample and tip, which is very difficult to quantify.[24] Therefore, the modification of the states in the tunnel junction by the applied bias is often neglected in simulated STM images.

It is possible to allow for some of these effects approximately[25] by including a transmission coefficient

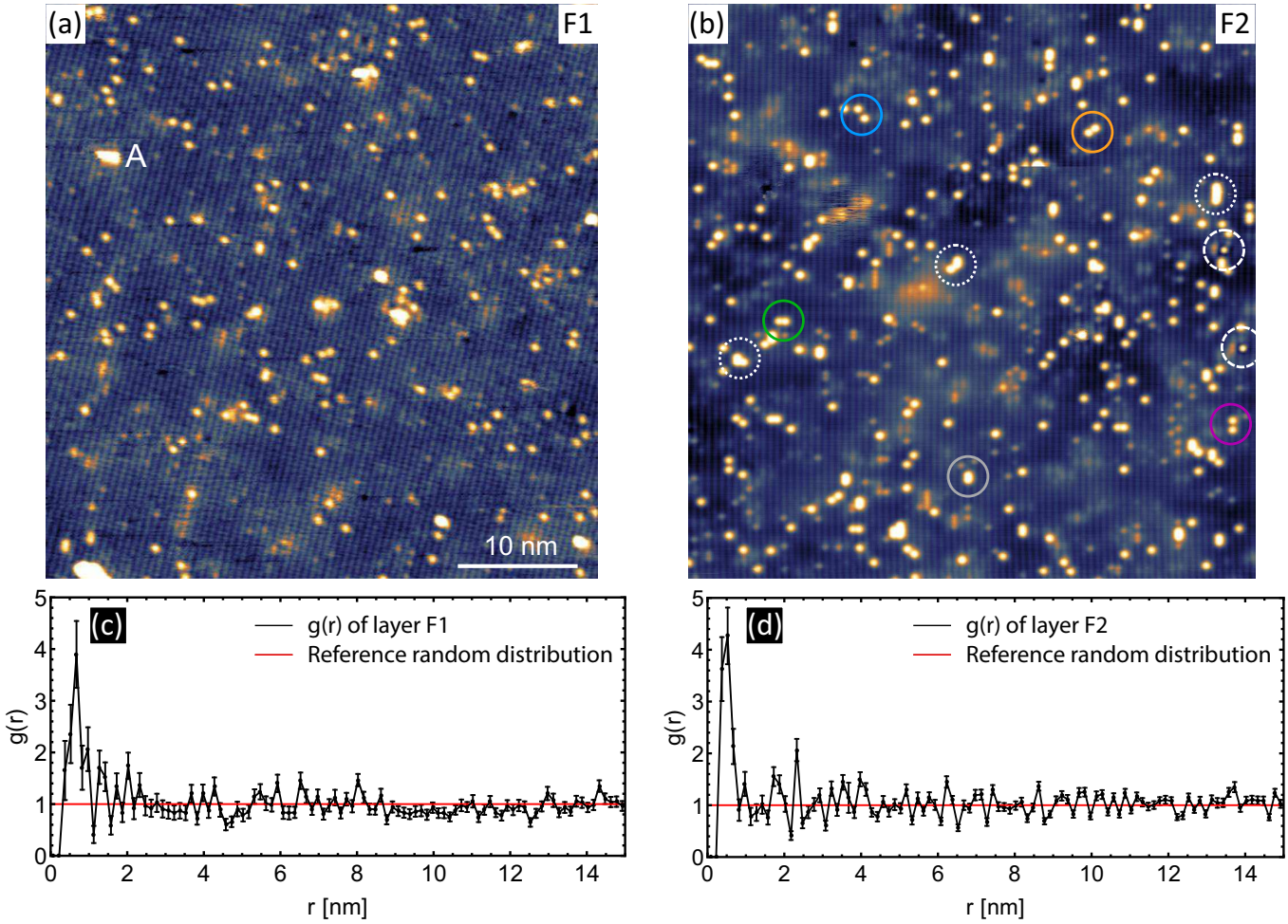

FIG. 3. (Color online) Filled state X-STM images of Bi:InP bulk layers F1 with an intented Bi content of 1.2 % (a) from sample A and F2 with an intended Bi concentration of 2.4 % (b) from sample B. F1 is imaged at $V_{bias} = -2.5$ V and $I_T = 40$ pA. F2 is imaged with the same I_T set point as F1 at $V_{bias} = -2.6$ V. The color functions of both X-STM images (a, b) are independently scaled for best visibility of the Bi-atoms in the surface. An adsorbate (A) is highlighted in (a) and in (b) 1^{st}, 2^{nd}, 3^{rd}, 4^{th}, and 6^{th} nearest neighbor Bi-pairs are marked with gray, green, orange, purple, and blue circles, respectively. Bi-clusters are indicated by white dotted circles and potential Bi_{In} antisites are marked with white dashed circles. Below the X-STM images (a, b) the corresponding PCFs of the Bi-atoms in the surface layer are shown (c, d).

in the density of states integral in Eq. 1. However, the effects are complicated and the exact form of the transmission coefficient is not known. In the present case, this analysis is not necessary because the image contrast depends strongly on the effective size and geometrical position of the surface atoms so only a qualitative prediction of the image contrast is needed to identify the origin of the image features. To verify this we have computed the bias voltage dependence of the image contrast and found that the qualitative form of the images typically persists over a wide bias voltage range. For example, in the case of Bi in the surface layer, the qualitative appearance of the filled states image remains the same over a range of at least 1 V.

B. Self organized Bi pair and cluster formation

For a better understanding of the unusually strong sub band gap photoluminescence of Bi:InP, which is proposed to be related to inhomogeneities in the Bi distribution,[4,9,11,12] knowledge about the local arrangement of Bi-atoms relative to each other is highly desirable. To explore this topic, two Bi:InP bulk layers F1 and F2 with intended Bi contents of 1.2 % and 2.4 % are investigated. In the following, only Bi_P-atoms in the

{110} surfaces are considered, because they are easily distinguishable from Bi-atoms in deeper layers or any other non Bi related objects (e.g. adsorbents or unintended dopants).

To quantitatively assess the relative spatial ordering of the Bi-atoms in the surface plane of layers F1 and F2 in Figure 3, the 2D pair-correlation function (PCF) for homogenous and isotropic systems

$$g(r) = \frac{1}{2\pi N \rho_0} \left\langle \frac{1}{r} \sum_{i \neq j}^{N} \delta(r - r_{ij}) \right\rangle \qquad (2)$$

is used.[26] The PCF gives a measure of the probability of finding a particle at a distance r from any other given particle. In equation 2, r_{ij} is the distance between particles i and j, ρ_0 is the average area number density, and N is the number of reference particles. A detailed description of the calculation of the PCF and the treatment of edge effects, which originate in the finite nature of the experimental data, is provided in section IV of the supplementary material.

The PCFs in Figures 3 (c, d) of layers F1 and F2 [Figures 3 (a, b)] are determined up to a maximum range of $R = 15$ nm with a sampling interval of $dr = 1.5$ Å. At smaller sampling intervals dr the statistics of the calculated PCFs would become especially at short distances too poor to be meaningful. Below the spacing of a first nearest neighbor anion pair in the (110) plane of $a_{InP}/\sqrt{2}$, where $a_{InP} = 5.86$ Å is the lattice constant of InP at 5 K, no other Bi-atoms can be found and the PCFs approach zero. In the range from 3 nm to 15 nm the convergence of the PCFs to unity indicates a completely, spatially random pattern (CSRP) of the Bi-atoms. Interestingly, on the short range there is a significantly increased probability of finding Bi-atoms close to each other in both layers F1 and F2. In particular, the probability of finding Bi-atoms in layer F1 with a spacing of (6.8 ± 0.8) Å is (3.9 ± 0.7) times and in layer F2 with a spacing of (5.3 ± 0.8) Å is (4.4 ± 0.6) times higher than for a CSRP. The region associated with an enhanced probability of another Bi-atom close by extends on average up to pair spacings of (9.8 ± 1.0) Å. At intermediate distances between 1 nm and 2 nm the PCF of F1 appears to oscillate in contrast to F1. We attribute these fluctuations to statistical noise, which is expected to be larger for F1 than for F2 because the Bi concentration in F1 is twice that in F2. This becomes particularly apparent at small radii, where the probability of finding a certain amount of Bi-atoms in the fixed sampling interval dr is lower than for larger distances.

The radial resolution, $dr = 1.5$ Å, of the PCFs in Figure 3 lies in the range of the length difference, $\Delta r = r_{n+1} - r_n$, between two successive n-th and $(n+1)$-th Bi-pairs. Here, r_n is the separation of the Bi atoms of the n-th nearest neighbor pair. For instance, first and second nearest neighbor pairs can just be resolved with a length difference of $\Delta r = 1.7$ Å. However, the length difference between any other n-th and $(n+1)$-th Bi-pairs can no longer be distinguished. Examples of the five closest n-th Bi-pairs with $n = 1, 2, 3, 4, 6$ are highlighted in Figure 3 (b) with solid circles. The 5^{th} nearest neighbor pair is not accessible in the {110} surfaces.

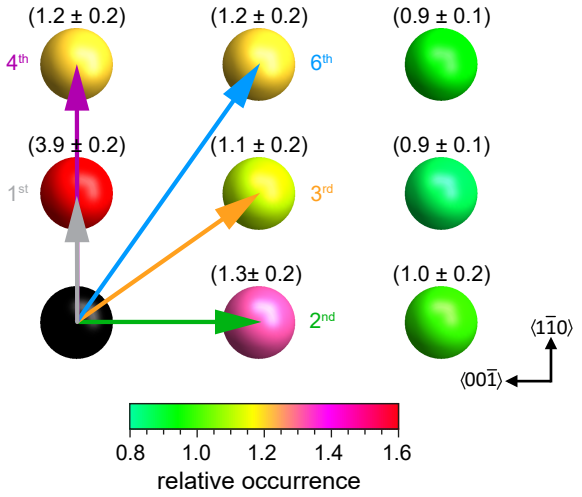

FIG. 4. (Color online) Relative occurrence distribution of neighboring Bi-atoms in the {110} surface planes, $p_{i,j}$, with a separation of up to two vertical and horizontal lattice constants from their partner at the left corner on the bottom. The statistics are based on a $(10.3 \pm 0.2) \times 10^3$ nm^2 large area of layer F2 in sample B. The color of the lattice sites represents the experimentally found populations relative to a comparable CSRP. Additionally, the exact values and errors are given above the grid positions. The orientation of the five closest n-th Bi-pairs in the (110) cleavage plane with $n = 1, 2, 3, 4, 6$ is illustrated by red arrows.

To further evaluate the short-range ordering in layer F2 of sample B at the atomic level a different approach is needed. Therefore, we determine the exact lattice positions of first layer Bi-atoms relative to each other on a maximum length scale of up to two lattice constants, (i, j), along the $\langle 1\bar{1}0 \rangle$ and $\langle 00\bar{1} \rangle$ directions. This is done for a much larger region of $(10.3 \pm 0.2) \times 10^3$ nm^2 than in Figure 3 (b). The experimental findings are compared to computationally-generated CSRPs with the same size and particle density as in the experiment. This results in a relative occurrence, $p_{i,j}$, which gives a measure for the probability of finding additional Bi-atoms on neighboring lattice sites. A detailed description of this analysis is provided in section V of the supplementary material. The results are summarized in the Figure 4, where the relative occurrence of neighboring Bi-atoms in the {110} surface, $p_{i,j}$, is displayed on a 3×3 lattice sites wide grid. In the lower left corner lies the reference position. Experiment and simulation are always the same at this point, which leads to a relative occurrence, $p_{0,0}$, of one. It is clear that there is an enhanced probability of finding a second Bi-atom in the neighboring shell on adjacent first and second nearest neighbor positions. Occupation of first nearest neighbor sites is with a relative occur-

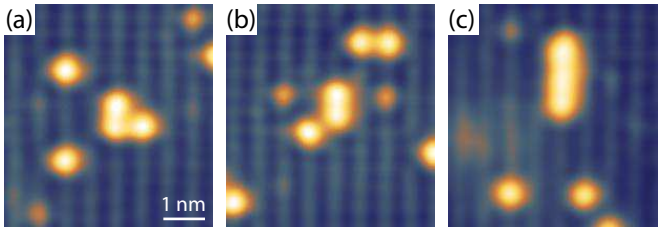

FIG. 5. (Color online) Filled state X-STM images of commonly observed Bi-cluster geometries, where the Bi-atoms are arranged in triangular (a), kinked (b), and linear (c) configurations. All cluster configurations (a, b, c) are presented in the same color range. The X-STM images are taken at $V_{bias} = -2.5$ V and $I_T = 40$ pA.

rence of (3.9 ± 0.2) strongly favorable. Second nearest neighbor positions are less favorable (relative occurrence of (1.3 ± 0.2)). This agrees with the frequent observation of first nearest neighbor Bi-pairs in layers F1 and F2 [see gray circles in Figure 3 (b)]

A visual assessment of layer F2 in Figure 3 (b) shows in addition to Bi-pairing the formation of small Bi-clusters, which is supported by the atomically resolved occurrence distribution in Figure 4. The individual atoms in these pairs and clusters lie on regular group-V lattice sites and are of comparable height to isolated Bi-atoms in the surface, confirming that they are Bi-related. In addition, identical pair and cluster geometries with weaker contrast than for Bi-atoms from the 3$^{\text{rd}}$ layer are found, which excludes a cleavage related origin. Commonly observed Bi-clusters consist mainly of a first nearest neighbor pair and an additional Bi-atom, which results in the triangular, kinked, and linear configurations shown Figures 5 (a, b, c). This suggests a connection with the strong trend towards first nearest neighbor Bi-pairing. Similarly, among the three different trimer configurations, linear arrangements are more often found than triangular and kinked geometries. Clusters with more than 4 Bi-atoms are rarely observed.

Our measurements confirm the formation of Bi-pairs and small Bi-clusters in Bi:InP grown at low temperatures, which were suggested in recent photoluminescence and DLTS studies on Bi:InP form the same reactor.[4,9,11,12] This further illustrates the importance of compositional order in dilute bismides. Pairs and clusters of Bi-atoms disturb the lattice more than single Bi-atoms, which potentially gives rise to additional states in the band gap near the valence band edge.[11,12,27] Configurational and environmental disorder are expected to broaden the states related to these arrangements of more than one Bi-atom.[28] Similarly, localized states in the band gap have been proposed for pairs and clusters of N-atoms.[29]

In STEM experiments on Bi:GaAs, areas with high probability for Bi-clustering are identified.[13] The 2D information provided in STEM studies represents, however, an average over the lamella thickness. Enhanced Bi concentrations in neighboring atomic columns do not directly prove that Bi-clustering occurs. The Bi-atoms in neighboring columns must not inevitably lie at the same depth in the lamella. EXAFS studies on Bi:GaAs show, consistent with our observations, indications for Bi-paring and Bi-clustering.[14] However, in the EXAFS investigation solely an enhanced trend towards first neighbor Bi-paring is reported, while here an enhanced occupation of neighboring sites beyond that level is found. Another difference lies in the wide range of Bi-cluster configurations found in the present work, which is more realistic than the solely tetrahedral arrangements of 4 first nearest neighbor Bi-pairs suggested by the EXAFS measurements.

There are indications for a possible connection between the atomic structure of the growth surface and the formation of Bi-pairs and Bi-clusters. For instance, Bi has an extraordinary strong tendency to segregate towards the surface. On the surface, Bi is poorly incorporated into the crystal and acts as a surfactant.[30] This can also lead to unintentional droplet formation.[31] One can imagine links between Bi-induced surface reconstructions and the enhanced tendency towards first nearest neighbor pairing.[32] For instance, the $CuPt_B$ ordering in highly doped $GaAs_{1-x}Bi_x$ was attributed to the dimerization of surface atoms.[33]

C. Crystal defects in Bi:InP

A general method for overcoming the poor solubility of Bi-atoms in MBE grown III-V compounds is to grow the material at a low temperature and at a low V/Bi flux ratio.[9,34,35] Unfortunately, these growth conditions favor the formation of group-III vacancies as well as group-V related antisites or interstitials.[36] We look for these defects in our Bi:InP samples.

1. In-vacancies

In the filled and empty state X-STM images in Figure 1, In-vacancies (V_{In}) can be found, which are identified with a white circle. A missing In-atom in the {110} surfaces affects the relaxed positions of its two neighboring surface P-atoms, which in consequence are shifted to slightly lower locations. In filled state images taken at high negative sample voltages this displacement gives rise to a dark contrast on two neighboring P-corrugation maxima, while in empty state images the missing In-atom appears as an atomic dark contrast at a local maximum of the In-corrugation. In X-STM images covering larger areas of the QW region further evidence for In-vacancies is found. Vacancies observed in X-STM measurements might originate either from the growth or the cleavage. Thermal In-desorption over time from the cleaved {110} InP surfaces is not an issue at 5 K and we never observed In-vacancy formation after cleavage.[37] No In-vacancies

are observed in the InP substrate, which supports a growth related origin of the In-vacancies in the epilayer region of sample B. The locations of the vacancies are not correlated with the nearby Bi-atoms. Bi-vacancy complexes, which could be an efficient way for releasing local strain induced by the large Bi-atoms, are not observed. The distinct but weak signature of In-vacancies cannot always reliably be detected in large filled state STM image, which hinders determination of their concentration.

2. *P-antisites*

In-vacancies, which act as acceptors, cannot be responsible for the observed n-type character at the epilayers of sample B. We suggest that this is due to the formation of phosphorus antisite defects (P_{In}), which can be expected in InP grown under group-V rich conditions at low temperatures.[12] Anion antisites in the {110} surfaces are electrically inactive and can be difficult to see in X-STM images. The weak but distinct signature of a P_{In} antisite in the surface appears in filled state X-STM images at low sample bias as an additional atomic state in between four surrounding group-V sites of changed morphology [Figure 6 (a)].[38] In empty state X-STM images [Figure 6 (b)] P_{In} antisites in the surface are confusingly similar to V_{In}. This can be understood in view of the smaller covalent radius of a P-atom compared to an In-atom.[39] Extended satellite-like features, which are characteristic for electrically active subsurface V_{III} antisites, could also be observed.[40,41] We estimate the content of P_{In} antisites in the surface of the QW region in sample B to be about $(1.6 \pm 0.4) \times 10^{11}$ cm^{-2}, which corresponds to a 3D concentration of $(6.7 \pm 2.5) \times 10^{16}$ cm^{-3}. This proves that the number of antisites is large, as was proposed in recent photoluminescence and DLTS studies on Bi:InP from the same reactor.[11,12]

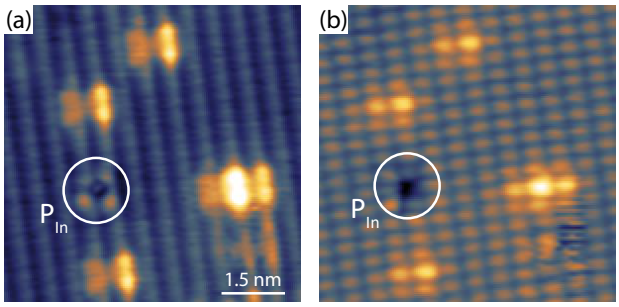

FIG. 6. (Color online) High resolution filled state (a) and empty state (b) X-STM images of a P_{In} antisite in the surface, which is marked with a white circle. The images are acquired from the same spot of QW 2 in sample B at $V_{bias} = -1.9$ V and $V_{bias} = 1.5$ V with the same $I_T = 30$ pA. The color ranges in both images are adjusted independently.

3. *Bi-antisites*

In filled state X-STM images of F2 in sample B with the highest Bi content addressed in this study, a fourth class (4) of features related to Bi is occasionally observed [see white dashed circles in Figures 3 (b) and 7], which occurs at lower frequency levels than classes $(0, 1, 2)$. These features appear at negative sample bias as a bright circle with a spatial extension of a single atom. In addition, this species is surrounded by a thin annulus, less than 3 Å wide, of negative contrast, which is followed by a region of positive contrast in the [100] growth direction. This long-ranged contrast appears to be too far from the atomic core of this feature to be of topographic origin and is rather reminiscent of electronic effects seen in X-STM images for donors and acceptors.[42–44] The appearance of class (3) has been verified with several physically different W-tips, which excludes any tip artifacts. The pure InP and Bi:InP bulk layers in the epilayer region of sample B are grown under the same conditions. Features (3) are only found in Bi:InP regions and not the pure InP epilayers. This strongly points to defects related to the incorporation of Bi-atoms rather than elements from the InP matrix. In addition, Bi-atoms are due to their large covalent radius compared to P-atoms more difficult to incorporate at higher concentrations. The pronounced atomic-like center of this Bi related defect lies between the P-rows, which suggests the possibilities of Bi interstitials or Bi_{In} antisites.

The formation energies of naturally existing point defects in InP, InAs and InSb have been investigated with DFT. The results show that anion interstitials in the bulk or on the {110} surfaces have, even under the most beneficial conditions, considerably higher formation energies than corresponding anionic V_{III} antisites.[36]. Therefore, we attribute class (3) to Bi_{In} substitutional atoms. In the closely related MBE grown Bi:GaAs system, Bi_{Ga} antisites have been reported and are believed to act as compensation centers for acceptors.[45] Based on atom counting, about (0.9 ± 0.3) % of the Bi-atoms of F2 in sample B are incorporated on group-III positions.

The atomic core of the Bi_{In} antisites is of comparable height to isovalent Bi_P atoms in the surface, which points to a position in the cleavage plane. Potential isovalent Bi_{In} antisites with valence three are excluded because of the long range contrast associated with this 4th class. The Bi_{In} double donor is, in consequence of the n-type environment and the additional tip induced band bending when addressing filled states (figure. 7), most likely imaged in its neutral state (D^0). The electrons are still bound to the D^0, which fits to the consistently observed long-range contrast of this feature. The surface plays a crucial role in X-STM measurements and the appearance of antisites in the surface differs greatly from sub surface layers. The physical and chemical properties of Bi-atoms and P-atoms, which lie at opposite ends of group-V, are considerably different. In X-STM images where both structural and electronic properties are

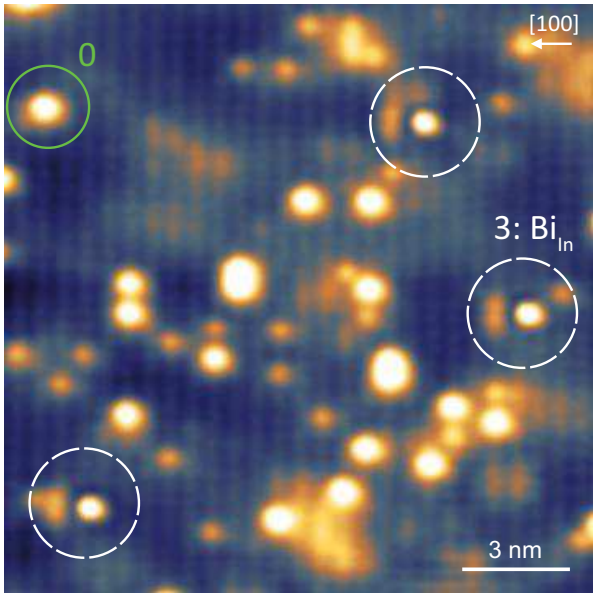

FIG. 7. (Color online) High resolution filled state X-STM image with potential Bi_{In} antisites (white dashed circles) with a valence of 5 in the surface layer in addition to commonly observed isovalent Bi_P substitutional atoms. An isovalent Bi_P atom in the first layer (0) is marked for comparison. The image is taken on F2 in sample B at $I_T = 40$ pA and $V_{bias} = -2.5$ V. The growth direction is indicated by an arrow.

probed, this may lead to differences in the appearance of P_{In} and Bi_{In} antisites.

Our observations support previous work, where P_{In} antisite defects in low temperature MBE grown Bi:InP are reported.[11,12] In addition, we show that V_{In} vacancies and potential Bi_{In} antisites are formed. Bi exhibits next to the valence of 5 a valence of 3 as in the case of Bi_2Te_3 and Bi_2Se_3. This implies that Bi can potentially function depending on its valence state on group-III substitutional positions as or a double donor (D) and on group-V sublattice positions as an isovalent impurity or a double acceptor (A).[46] X-STM, which is also sensitive to the local electronic properties of single impurities, is an ideal tool to address all these potential configurations of single Bi atoms. In this work, no indications for Bi-atoms with a valence of three on either group-III or group-V sites are found.

IV. CONCLUSION

Dilute III-V-bismides have a great deal of potential for innovative device applications, however these materials still suffer from a range of problems related to short range ordering and defect formation. In this work we have demonstrated the suitability of using X-STM to investigate these problems, in real space at the atomic level.

In Bi:InP we have identified isovalent Bi_P-atoms down to the second monolayer below the {110} InP surfaces by comparing X-STM measurements to complementary DFT calculations. We have shown that the contrast observed in the X-STM measurements taken at high negative U_S can be understood by considering the geometry of the relaxed (110) surface which, in turn, is determined primarily by the difference in effective size of the Bi dopant compared to the In and P atoms. Bi is the largest stable group V element and, using this geometrical model,[18] we therefore predict similar contrast in any Bi-doped III-V compound with a zinc-blende structure.

In bulk Bi:InP layers we observed a strongly enhanced tendency for first nearest neighbour Bi-pairing. This tendency explains the geometry of the trimers and small clusters of Bi-atoms that we also observed. We suggest these Bi-pairs and Bi-clusters are candidates for the unusual sub band-gap emission reported previously for Bi:InP.[4,9,11,12]

In our measurements we see no evidence for the incorporation of Bi-atoms on group-III or group-V sublattice sites with a valence of three. If this type of crystal defect exists, its density must be rather low ($< 5 \times 10^{15}$ cm^{-3}). Crystal defects, such as V_{In} vacancies, P_{In} antisites, and potential Bi_{In} antisites, are still an issue in Bi:InP despite the considerable progress in the growth of crystalline III-V compounds containing Bi.

These results give important insights into the structural properties of state of the art Bi doped InP. This is essential for a better understanding of the unusual optoelectronic properties of Bi:InP and helps to further develop this material system towards the quality of GaAs based materials. In addition, the identification of Bi atoms down to the second layer below the surface provides the basis for further scanning tunneling spectroscopy studies of the impurity states of individual Bi atoms and Bi clusters.

CMK and PMK thank NanoNextNL, a micro and nanotechnology consortium of the Government of the Netherlands and 130 partners for financial support. FJT thanks the University of Leicester for award of a research studentship. The DFT calculations were performed on the ALICE High Performance Computing Facility at the University of Leicester. LYZ, KW, YYL and SMW acknowledge the National Basic Research Program of China (Grant No. 2014CB643902) and the Key Program of Natural Science Foundation of China (Grant No. 61334004) for financial support.

* c.m.krammel@tue.nl

[1] Y. Zhang, A. Mascarenhas, and L.-W. Wang, Phys. Rev. B **71**, 155201 (2005).
[2] B. Fluegel, S. Francoeur, A. Mascarenhas, S. Tixier, E. C.

Young, and T. Tiedje, Phys. Rev. Lett. **97**, 067205 (2006).
[3] M. Usman, C. A. Broderick, A. Lindsay, and E. P. O'Reilly, Phys. Rev. B **84**, 245202 (2011).
[4] Y. Gu, K. Wang, H. Zhou, Y. Li, C. Cao, L. Zhang, Y. Zhang, Q. Gong, and S. Wang, Nanoscale Research Letters **9**, 1 (2014).
[5] S. Francoeur, M.-J. Seong, A. Mascarenhas, S. Tixier, M. Adamcyk, and T. Tiedje, Appl. Phys. Lett. **82**, 3874 (2003).
[6] S. Tixier, M. Adamcyk, T. Tiedje, S. Francoeur, A. Mascarenhas, P. Wei, and F. Schiettekatte, Appl. Phys. Lett. **82**, 2245 (2003).
[7] S. P. Svensson, H. Hier, W. L. Sarney, D. Donetsky, D. Wang, and G. Belenky, J. Vac. Sci. Technol. B **30**, 02B109 (2012), http://dx.doi.org/10.1116/1.3672023.
[8] I. C. Sandall, F. Bastiman, B. White, R. Richards, D. Mendes, J. P. R. David, and C. H. Tan, Appl. Phys. Lett. **104**, 171109 (2014), http://dx.doi.org/10.1063/1.4873403.
[9] K. Wang, Y. Gu, H. F. Zhou, L. Y. Zhang, C. Z. Kang, M. J. Wu, W. W. Pan, P. F. Lu, Q. Gong, and S. M. Wang, Sci. Rep. **4**, 5449 (2014).
[10] W. Pan, P. Wang, X. Wu, K. Wang, J. Cui, L. Yue, L. Zhang, Q. Gong, and S. Wang, J. All. Com. **656**, 777 (2016).
[11] X. Wu, C. Xiren, W. Pan, P. Wang, L. Zhang, Y. Li, H. Wang, K. Wang, J. Shao, and S. Wang, Sci. Rep. **6**, 27867 (2016).
[12] L. Gelczuk, H. Stokowski, J. Kopaczek, L. Zhang, Y. Li, K. Wang, P. Wang, S. Wang, and R. Kudrawiec, J. Phys. D: Appl. Phys. **49**, 115107 (2016).
[13] D. L. Sales, E. Guerrero, J. F. Rodrigo, P. L. Galindo, A. Yáñez, M. Shafi, A. Khatab, R. H. Mari, M. Henini, S. Novikov, M. F. Chisholm, and S. I. Molina, Appl. Phys. Lett. **98**, 101902 (2011).
[14] G. Ciatto, E. C. Young, F. Glas, J. Chen, R. A. Mori, and T. Tiedje, Phys. Rev. B **78**, 035325 (2008).
[15] X. Gonze, B. Amadon, P.-M. Anglade, J.-M. Beuken, F. Bottin, P. Boulanger, F. Bruneval, D. Caliste, R. Caracas, M. Côté, T. Deutsch, L. Genovese, P. Ghosez, M. Giantomassi, S. Goedecker, D. Hamann, P. Hermet, F. Jollet, G. Jomard, S. Leroux, M. Mancini, S. Mazevet, M. Oliveira, G. Onida, Y. Pouillon, T. Rangel, G.-M. Rignanese, D. Sangalli, R. Shaltaf, M. Torrent, M. Verstraete, G. Zerah, and J. Zwanziger, Computer Phys. Commun. **180**, 2582 (2009).
[16] X. Gonze, G.-M. Rignanese, M. Verstraete, J.-M. Beuken, Y. Pouillon, R. Caracas, F. Jollet, M. Torrent, G. Zerah, M. Mikami, P. Ghosez, M. Veithen, J.-Y. Raty, V. Olevano, F. Bruneval, L. Reining, R. Godby, G. Onida, D. Hamann, and D. Allanr, Z. Kristallogr. **220**, 558 (2005).
[17] `http://www.abinit.org/downloads/psp-links/psp-links/lda_fhi`, accessed: 2016-03-30.
[18] F. J. Tilley, M. Roy, P. A. Maksym, P. M. Koenraad, C. M. Krammel, and J. M. Ulloa, Phys. Rev. B **93**, 035313 (2016).
[19] J. Tersoff and D. R. Hamann, Phys. Rev. B **31**, 805 (1985).
[20] J. Tersoff and D. R. Hamann, Phys. Rev. Lett. **50**, 1998 (1983).
[21] J. Bardeen, Phys. Rev. Lett. **6**, 57 (1961).
[22] P. Ebert, B. Engels, P. Richard, K. Schroeder, S. Blügel, C. Domke, M. Heinrich, and K. Urban, Phys. Rev. Lett. **77**, 2997 (1996).
[23] N. Ishida, K. Sueoka, and R. M. Feenstra, Phys. Rev. B **80**, 075320 (2009).
[24] C. J. Chen, J. Vac. Sci. Technol. A **6**, 319 (1988), http://dx.doi.org/10.1116/1.575444.
[25] R. Wiesendanger, *Scanning Probe Microscopy and Spectroscopy: Methods and Applications*, Scanning Probe Microscopy and Spectroscopy: Methods and Applications (Cambridge University Press, 1994) p. 109.
[26] C. Janot, *QUASICRYSTALS. A Primer, 2nd edition, édition en anglais:*, Monographs on the physics and chemistry of materials (Clarendon Press, 1997).
[27] M. Usman, C. A. Broderick, A. Lindsay, and E. P. O'Reilly, Phys. Rev. B **84**, 245202 (2011).
[28] L. C. Bannow, O. Rubel, S. C. Badescu, P. Rosenow, J. Hader, J. V. Moloney, R. Tonner, and S. W. Koch, Phys. Rev. B **93**, 205202 (2016).
[29] P. R. C. Kent and A. Zunger, Appl. Phys. Lett. **79**, 2339 (2001).
[30] E. Young, S. Tixier, and T. Tiedje, Journal of Crystal Growth **279**, 316 (2005).
[31] P. T. Webster, N. A. Riordan, C. Gogineni, S. Liu, J. Lu, X.-H. Zhao, D. J. Smith, Y.-H. Zhang, and S. R. Johnson, J. Vac. Sci. Technol. B **32**, 02C120 (2014).
[32] A. Duzik, J. C. Thomas, A. van der Ven, and J. M. Millunchick, Phys. Rev. B **87**, 035313 (2013).
[33] A. G. Norman, R. France, and A. J. Ptak, J. Vac. Sci. Technol. B **29**, 03C121 (2011), http://dx.doi.org/10.1116/1.3562512.
[34] J. Li, T.-H. Kim, K. Forghani, W. Jiao, W. Kong, K. Collar, T. F. Kuech, and A. S. Brown, J. Appl. Phys. **116**, 043524 (2014), http://dx.doi.org/10.1063/1.4891874.
[35] R. B. Lewis, M. Masnadi-Shirazi, and T. Tiedje, Appl. Phys. Lett. **101**, 082112 (2012), http://dx.doi.org/10.1063/1.4748172.
[36] A. Höglund, C. W. M. Castleton, M. Göthelid, B. Johansson, and S. Mirbt, Phys. Rev. B **74**, 075332 (2006).
[37] P. Ebert, M. Heinrich, M. Simon, K. Urban, and M. G. Lagally, Phys. Rev. B **51**, 9696 (1995).
[38] P. Ebert, P. Quadbeck, K. Urban, B. Henninger, K. Horn, G. Schwarz, J. Neugebauer, and M. Scheffler, Appl. Phys. Lett. **79**, 2877 (2001).
[39] P. Pyykkö and M. Atsumi, Chem. - Eur. J. **15**, 168 (2009).
[40] R. M. Feenstra, J. M. Woodall, and G. D. Pettit, Phys. Rev. Lett. **71**, 1176 (1993).
[41] R. B. Capaz, K. Cho, and J. D. Joannopoulos, Phys. Rev. Lett. **75**, 1811 (1995).
[42] R. M. Feenstra, G. Meyer, F. Moresco, and K. H. Rieder, Phys. Rev. B **66**, 165204 (2002).
[43] Z. F. Zheng, M. B. Salmeron, and E. R. Weber, Appl. Phys. Lett. **64**, 1836 (1994).
[44] A. M. Yakunin, A. Y. Silov, P. M. Koenraad, J. H. Wolter, W. Van Roy, J. De Boeck, J.-M. Tang, and M. E. Flatté, Phys. Rev. Lett. **92**, 216806 (2004).
[45] R. N. Kini, A. J. Ptak, B. Fluegel, R. France, R. C. Reedy, and A. Mascarenhas, Phys. Rev. B **83**, 075307 (2011).
[46] G. Ciatto, P. Alippi, A. A. Bonapasta, and T. Tiedje, Appl. Phys. Lett. **99**, 141912 (2011), http://dx.doi.org/10.1063/1.3647635.
[47] G. J. Sullivan, A. Ikhlassi, J. Bergman, R. E. DeWames, J. R. Waldrop, C. Grein, M. Flatté, K. Mahalingam, H. Yang, M. Zhong, and M. Weimer, J. Vac. Sci. Technol. B **23**, 1144 (2005).
[48] H. A. McKay, R. M. Feenstra, T. Schmidtling, U. W. Pohl, and J. F. Geisz, J. Vac. Sci. Technol. B **19**, 1644 (2001).
[49] C. J. Chen, Phys. Rev. Lett. **65**, 448 (1990).